Solar Energy 254 (2023) 67–72

Contents lists available at ScienceDirect

Solar Energy

journal homepage: www.elsevier.com/locate/solener

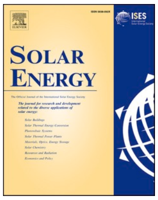

Structural and optical properties of Sb_xSe_y thin films obtained by chemical molecular beam deposition method from Sb and Se precursors

T.M. Razykov [a], J. Bekmirzoev [a], A. Bosio [b], B.A. Ergashev [a,*], D. Isakov [a], R. Khurramov [a], K.M. Kouchkarov [a], M.A. Makhmudov [a], A. Romeo [c], N. Romeo [b], M.S. Tivanov [d,*], Sh.B. Utamuradova [e], D.S. Bayko [d], L.S. Lyashenko [d], O.V. Korolik [d], A.A. Mavlonov [f]

[a] *Physical-Technical Institute, Chingiz Aytmatov Street 2B, Tashkent 100084, Uzbekistan*
[b] *University of Parma, G. P Usberti 7/A – 43124, Parma, Italy*
[c] *Universita' di Verona, Ca' Vignal 2- Strada Le Grazie 15, 37134 Verona, Italy*
[d] *Faculty of Physics, Belarusian State University, 220030 Minsk, Belarus*
[e] *Institute of Semiconductors Physics and Microelectronics, Yangi Olmazor Street 20, Tashkent 100057, Uzbekistan*
[f] *Research Organization of Science and Technology, Ritsumeikan University, 1-1-1 Nojihigashi, Kusatsu, Shiga 525-8577, Japan*

ARTICLE INFO

Keywords:
Sb_2Se_3
Chemical molecular beam deposition (CMBD)
X-ray analysis
Raman spectroscopy
Atomic force microscopy
Solar cell materials

ABSTRACT

Sb_xSe_y thin-films were obtained by chemical-molecular beam deposition (CMBD) on soda-lime glass from Sb and Se precursors. By the precise control of the Sb/Se ratio, Sb_2Se_3 thin films with stoichiometric composition were successfully obtained. The elemental and phase composition, as well as the crystal structure of Sb_xSe_y thin-films, were studied by energy-dispersive X-ray microanalysis, X-ray diffraction, Raman spectroscopy, scanning electron microscopy and atomic force microscopy. The optical bandgap of the films was determined from the absorption spectra acquired by a spectrophotometer. The physical properties of Sb_xSe_y thin films with different compositions were investigated.

1. Introduction

Among binary composite semiconductors, antimony selenide Sb_2Se_3 has been intensively studied over the last decade as an absorbing layer for thin-film solar cells since it has a strong absorption of sunlight $\alpha > 10^5$ (Zhou et al., 2014) and an optimal band gap of 1.1–1.3 eV for a single-junction solar element (Chen et al., 2017; Spalatu et al., 2021). The one-dimensional ribbon structure of $(Sb_4Se_6)_n$ has strong anisotropic properties (Kim et al., 2017; Zhou et al., 2015) and high theoretical conversion efficiency (31% according to the Shockley–Queisser detailed balance model) (Rühle, 2016) providing excellent properties. In addition, the elements that make up these materials have a relatively low cost, with amphibious Sb and Se with contents of 0.2 and 0.05 ppm (parts per million), respectively, resistance to external influences and nontoxicity (Zeng et al., 2016). At present, the efficiency of thin film solar cells based on Sb_2Se_3 in a nonplanar configuration is 9.2% (Li et al., 2019). The efficiency of an Sb_2Se_3 solar cell is highly dependent on the physical properties of the base layer as well as the growth method. Sb_2Se_3 films have been synthesized by various methods (rapid vacuum thermal evaporation (Wang et al., 2017), magnetron sputtering (Ma et al., 2019), chemical bath deposition (Maghraoui-Meherzi et al., 2013), pulsed laser deposition (Mavlonov et al., 2020b) etc.), but all these methods required additional processes to improve the physical properties, such as selenization and subsequent annealing (structural, morphological and optical) of the absorbing layer. In our method, we can obtain different compositions of thin films without additional procedures by changing the temperature of the precursors during growth.

Due to the ribbon-like structure and 1-D conductivity, in the literature, Sb_2Se_3 films with crystal orientation (hk1) were more efficient for application in photovoltaics, while (hk0) was less efficient (Chen et al., 2017; Li et al., 2019; Razykov et al., 2019). Therefore, by varying the synthesis conditions and methods, it is possible to obtain highly efficient Sb_2Se_3 thin films with the texture required for solar cells. Such a structure induces anisotropic optical and electrical properties. The film surface morphology also differs, greatly depending on the conditions (substrate and source/source temperatures) and the synthesis method (Chen et al., 2017; Mavlonov et al., 2020b).

---

* Corresponding authors.
E-mail addresses: bobur_7007@yahoo.com (B.A. Ergashev), michael.tivanov@gmail.com (M.S. Tivanov).

https://doi.org/10.1016/j.solener.2023.03.010
Received 14 January 2023; Received in revised form 2 March 2023; Accepted 5 March 2023

2. Experimental

2.1. Fabrication of thin films

Sb_xSe_y layers were deposited by chemical molecular beam deposition (CMBD). A schematic representation of the CMBD method is shown in Fig. 1. In the presence of 99.999% high purity Sb and Se beads. Soda-lime glass (SLG) was used as a substrate. The SLG substrates were cleaned with detergent, acetone, ethanol, and deionized water in an ultrasonic bath and finally dried with a stream of N_2 gas. The Sb and Se granules were placed separately on quartz crucibles in an evaporation chamber. Quartz crucibles were subjected to heat treatment from special molybdenum heaters, and Sb and Se granules were melted and evaporated from the crucibles at atmospheric pressure with gaseous hydrogen at a flow rate of 20 cm^3/min. Sb_xSe_y thin films with a substrate temperature of 500 °C were obtained at Sb 950–1000 °C and Se 480–500 °C at an evaporation time of 30 min. The 2–3 μm thickness of the thin films was determined using a MIM-7 microscope.

At the Sb (950–1000 °C) and Se (480–500 °C) evaporation temperatures, granules transfer into the vapour phase (Eq. (1)):

$$Sb(s) + 2Se(s) + H_2 = Sb(g) + Se_2(g) + H_2 \quad (1)$$

Se_2 (g) reacts with hydrogen, and hydrogen selenide is formed (Eq. (2)):

$$Se_2(g) + 2H_2 = 2H_2Se(g) \quad (2)$$

Sb and Se atoms and H_2Se molecules cover the surface of the substrate, and Sb_xSe_y films are formed as a consequence of their interaction (Eq. (3)):

$$3xSb(g) + ySe_2(g) + H_2Se(g) = 3Sb_xSe_y(s) + H_2 \quad (3)$$

The composition of Sb_xSe_y films was controlled by changing the Sb/Se ratio in the vapour phase mixture of Sb and Se (evaporated amount), which was varied by the molecular beam intensities of Sb and Se.

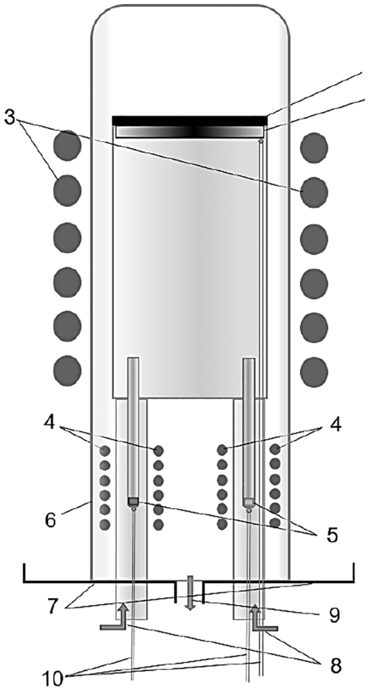

Fig. 1. Schematic representation of the CMBD method for obtaining Sb_xSe_y thin films. 1, 2 – substrate and holder, 3 – substrate heater, 4 – source heaters, 5 – crucibles of evaporated components, 6 – reactor cap, 7 – flange, 8 – gas inlet, 9 – gas outlet, 10 – thermocouples.

2.2. Measurement and characterization

We analysed Sb_xSe_y thin films using various techniques to determine how different ratios of Sb/Se affected the crystal structure, morphology, and optical properties of the films. The crystal structure was performed by using an Ultima IV (Rigaku) X-ray diffractometer in the grazing incidence diffraction geometry (GIXD) at 1 degree of incident X-rays with CuKα radiation source (λ = 1.54178 Å). XRD analysis was carried out with the use of the database of the Joint Committee on Powder Diffraction Standard (JCPDS) and Crystallography Open Database (COD). Raman spectra were measured at room temperature, using a Nanofinder HE (LOTIS TII) confocal spectrometer. A solid-state laser, with a radiation wavelength of 532 nm, was used to excite. The power of laser radiation incident on the samples was reduced to 60 μW, to avoid thermal damage. Spectral resolution was better, than 2.5 cm^{-1}. The size of the area, on which the laser radiation was focused on the surface of the samples, was about 0.7 μm in diameter. The surface morphology and topography were investigated by using a LEO-1455 VP (Carl Zeiss) scanning electron microscope (SEM) and a Solver Nano (NT-MDT) atomic force microscope (AFM). The AFM instrument was used in the semi-contact mode, with a scanning probe of 10 nm tip radius, at a resonance frequency of 236 kHz. The chemical composition was determined by energy dispersive X-ray (EDX) analysis using an Aztec Energy Advanced X-Max 80 (Oxford Instruments) spectrometer. The absorption spectra of the films were acquired by a spectrophotometer UV-1280 (Shimadzu).

3. Results and discussions

To determine the composition of the grown films, EDX analysis was carried out (see Fig. 2). According to the EDX analysis, the Sb/Se ratio in the films was 0.66, 0.73, and 0.85. And found a direct linear dependence between the ratio of the flow of raw materials in the vapour phase and the composition of the obtained film (solid phase). Such a linear dependence makes it quite easy to form films of a given composition.

The surface morphology was investigated using SEM imaging. Fig. 3 (a, b, c) shows the surface morphology of Sb_xSe_y thin films on SLG at a substrate temperature of 500 °C. All Sb_xSe_y thin films exhibited compact surface morphology. The grain sizes of Sb_xSe_y thin films, which consist of a dense columnar structure at an angle from 0° to 60° to the substrate, were between 0.5 ÷ 10 μm. Average diameters and lengths of Sb_xSe_y rods deposited at 0.66 and 0.73 Sb/Se ratios were nearly the same at 2 ÷ 5 μm and 0.5 ÷ 2 μm, respectively. At a 0.85 ratio, the length of the rods was between 4 and 10 μm. The size of Sb_xSe_y rods are larger with the

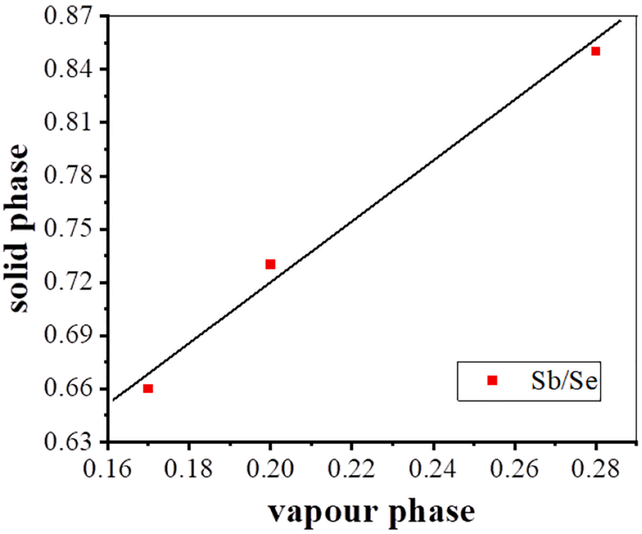

Fig. 2. Dependency of Sb/Se ratios in vapour and solid phases.

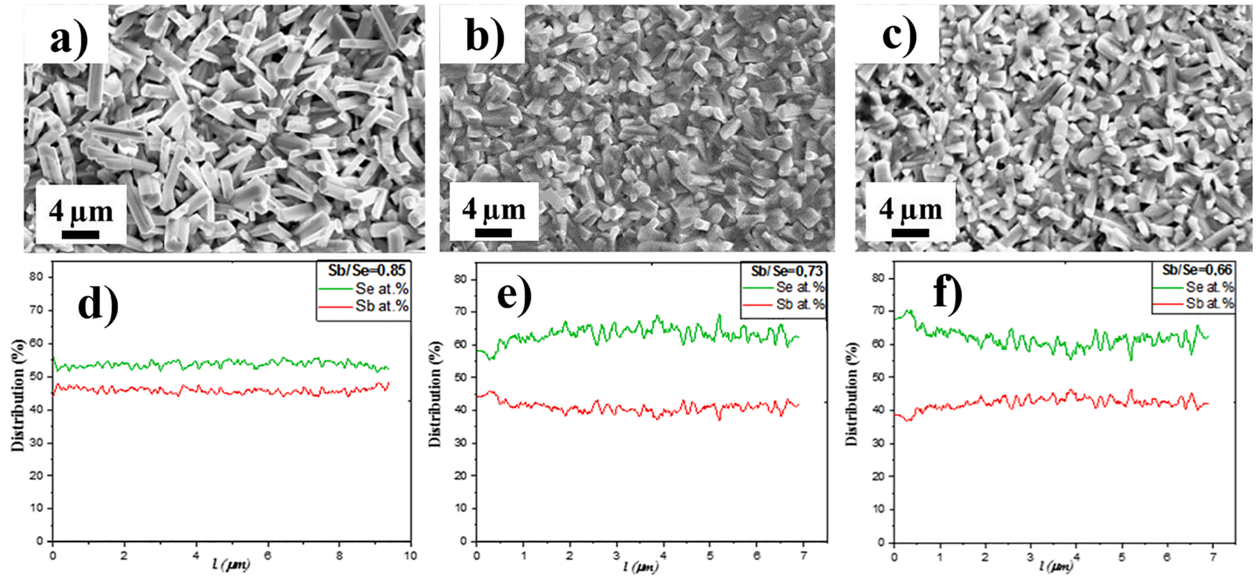

Fig. 3. (a, b, c) SEM images of Sb_xSe_y thin films deposited at (a) 0.85, (b) 0.73 and (c) 0.66 Sb/Se ratio by the CMBD method. (d, e, f) The distribution of Sb and Se contents among the exact lines on the sample surface at the atomic percentage.

increase of Sb/Se ratio. This result suggested that a lower percentage of Se atoms in the Sb_xSe_y thin films leads to a larger grain size in the Sb/Se ratio range of 0.66–0.85.

Additionally, the distribution of Sb and Se contents among the exact lines on the film surface were determined by EDX measurements. As shown in Fig. 3 (d, e, f), Sb and Se atoms were distributed stably.

As the ratio Sb/Se approaches the stoichiometric, long rods turn into shorter and smoother grains. From these EDX data, it was observed that the increase in Se content in the solid phase was directly proportional to the Se content in the vapour phase during the growth process.

Surface morphology-like average surface roughness studies carried out using atomic force microscopy (Fig. 4) showed that Sb_xSe_y films have a developed surface relief in the range of ~ 0.4–0.7 µm. All AFM parameters for Sb_xSe_y films are given in Table 1. The average and root-mean-square roughness of the surface decreases with the approach to the stoichiometric ratio. When the surface skewness increases from the characteristic values of the normal distribution (zero skewness reflects symmetrical height distribution) to a value of 0.44. This corresponds to the prevalence of surface peaks over valleys and may indicate the observation of a profile with filled valleys (Gadelmawla et al., 2002). The values of the kurtosis for the stoichiometric ratio correspond to the normal character of sharpness of the surface height distribution (Ska ~ 3). And for selenium-depleted films, the surface has a platykurtoic character (Gadelmawla et al., 2002).

Table 1
AFM data for Sb_xSe_y thin films with different compositions.

Samples (Sb/Se)	0.85	0.73	0.66
Roughness average Sa, um	0.72	0.46	0.43
Root Mean Square Roughness Sq, um	0.89	0.56	0.55
Skewness Ssk	0.10	0.13	0.44
Kurtosis Ska	2.78	2.77	3.08

GIXD measurements were taken on different samples to establish the phase composition and determine the preferred orientation of Sb_xSe_y layers. As shown in Fig. 5a, all diffraction lines belong to orthorhombic Sb_2Se_3 phase (JCPDS 15–0861). The obtained diffraction patterns are in good agreement with the standard pattern, indicating good crystallinity of the films, while no other phases were detected. Virtually no noticeable change in texture is observed for the different Sb/Se ratios, consistent with the apparent stability of the synthesis process up to this point.

It is known that Sb_2Se_3 films consist of one-dimensional $(Sb_4Se_6)_n$ ribbons stacked along the [0 0 1] direction due to Sb-Se covalent bonds, while $(Sb_4Se_6)_n$ ribbons are held together by Van der Waals forces between the ribbons (Deringer et al., 2015; Filip et al., 2013; Zhou et al.,

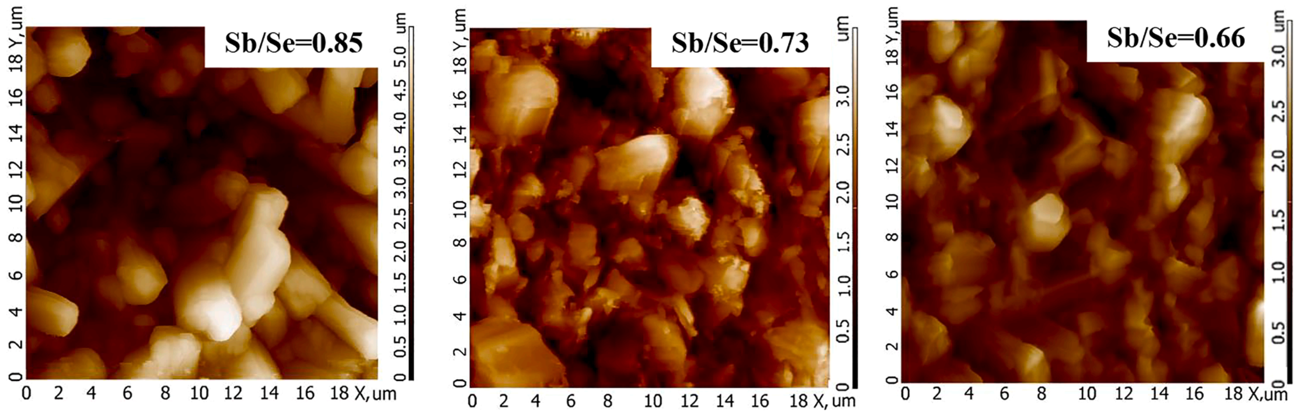

Fig. 4. AFM images of Sb_xSe_y thin films with different compositions.

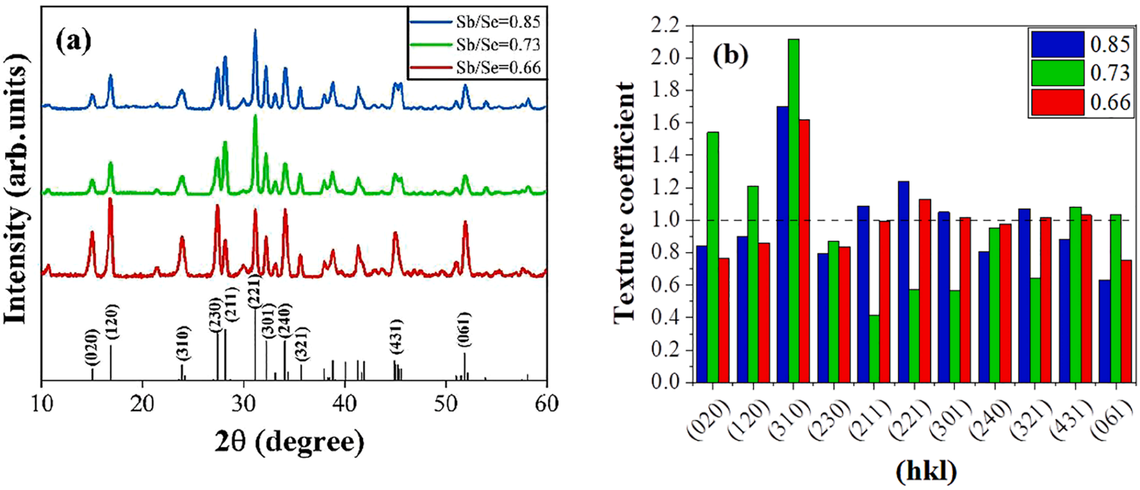

Fig. 5. (a) GIXD patterns and (b) the texture coefficients of the diffraction peaks of the Sb_xSe_y thin films deposited at different Sb/Se ratios.

2015). To analyze the change in texture, 11 lines were selected that have the highest intensity: (0 2 0), (1 2 0), (1 3 0), (2 3 0), (2 1 1), (2 2 1), (3 0 1), (2 4 0), (3 2 1), (4 3 1), (0 6 1). To determine the difference in orientations of thin films deposited at different Sb/Se ratios, the texture coefficient (*TC*) of different oriented peaks of samples was calculated by the following Eq. (4) (Li et al., 2017):

$$TC_{(hkl)} = \frac{\frac{I(hkl)}{I_0(hkl)}}{\frac{1}{N}\sum_{i=1}^{N}\frac{I(h_ik_il_i)}{I_0(h_ik_il_i)}}, \tag{4}$$

where *I(hkl)* and $I_0(hkl)$ are the diffraction peak intensities of the *(hkl)* planes in the measured and standard XRD patterns of Sb_2Se_3 (JCPDS 15–0861), respectively; *N* is the total number of orientations considered for the calculation. A larger *TC* value indicated a preferred orientation of the grain along this direction (Fig. 5b).

For the Sb_xSe_y thin films prepared at a stoichiometric Sb/Se ratio of 0.66, the intensity of the peaks (*hk*1) is stronger than that of the peaks (*hk*0) – for samples with the Sb/Se ratios of 0.73 and 0.85. The ratio of the sum of TC lines (*hk*1) such as (2 1 1), (2 2 1), (3 0 1), (3 2 1) and (0 6 1) to the sum of TC lines (*hk*0) such as (0 2 0), (1 2 0), (1 3 0), (2 3 0) and (2 4 0), is equal to 1.2. Accordingly, peaks with the preferred orientation (*hk*1) are dominant, which are attributed to vertically oriented ribbons. Among the orientations (*hk*1), the preferred orientations (2 1 1) and (2 2 1) became more intense. (*hk*1)-Oriented grains, consisting of $(Sb_4Se_6)_n$ ribbons, have a certain angle of inclination with the substrate, which has the best carrier transport ability (Guo et al., 2019). It can be imagined that the transfer of carriers in the direction of the preferred (*hk*1) orientation will be easier than in the direction of the (*hk*0) orientation, which prevents the movement of carriers through the volume.

In addition, theoretical calculations have shown that the formation energy varies depending on the crystal orientations. For example, the (*hk*0) orientations, i.e. corresponding to the (1 1 0) and (1 2 0) planes, have lower formation energies compared to other crystal orientations because of the absence of dangling bonds in the (*hk*0) orientations (Mavlonov et al., 2020a; Zhang et al., 2021). As a result, these preferred orientations have been found to be useful for designing high-performance Sb_2Se_3-based solar cells (Choi et al., 2014; Wen et al., 2018) due to less recombination and improved carrier transport due to its soft grain boundaries and better carrier transport capability. Thus, the Sb_2Se_3 films exhibited strong anisotropy. This unique trend appears to be related to the anisotropic properties of the one-dimensional crystal structure of Sb_2Se_3 (Lei et al., 2019).

Raman scattering measurements were performed for more details about the structure of Sb_xSe_y thin films deposited at different Sb/Se ratios, as indicated in Fig. 6. As seen from the figure, the Raman spectra display peaks at approximately 80, 100, 126, 145, 153, 190, 211, 237 and 441 cm^{-1}. The peaks at approximately 80, 100, 126, 153, 190, and 211 cm^{-1} are commonly reported and assigned to the Sb_2Se_3 phase (Kumar et al., 2021; Lei et al., 2019; Shongalova et al., 2018a). The peak at about 153 cm^{-1} has been attributed to the A_{2u} mode of the Sb–Sb bond (Lei et al., 2019), while the peaks at about 190 and 211 cm^{-1} are commonly assigned to the A_g mode of the Sb–Se–Sb bending vibrations of Sb_2Se_3 (Kumar et al., 2021; Shongalova et al., 2018a). In (Vidal-Fuentes et al., 2019), the peaks at 80 and 100 cm^{-1} are also designated as A_g vibrations. The sample with an Sb/Se = 0.66 ratio exhibits peaks at 80, 145, 237 cm^{-1} (441 cm^{-1} is second order of 237 cm^{-1}), which are attributed to the trigonal Se stretching vibration mode in Sb_2Se_3 (Nagata et al., 1981; Shongalova et al., 2018b; Vidal-Fuentes et al., 2019), which agrees with elemental analysis of this samples.

The corresponding Tauc plots for the Sb_xSe_y thin films are shown in Fig. 7a. The optical band gap (E_g) of samples can be calculated according to the Tauc formula (Eq. (5)) (Yang et al., 2020):

$$(\alpha h\nu)^n = A(h\nu - E_g) \tag{5}$$

where α is the absorption coefficient, $h\nu$ is the photon energy, A is a

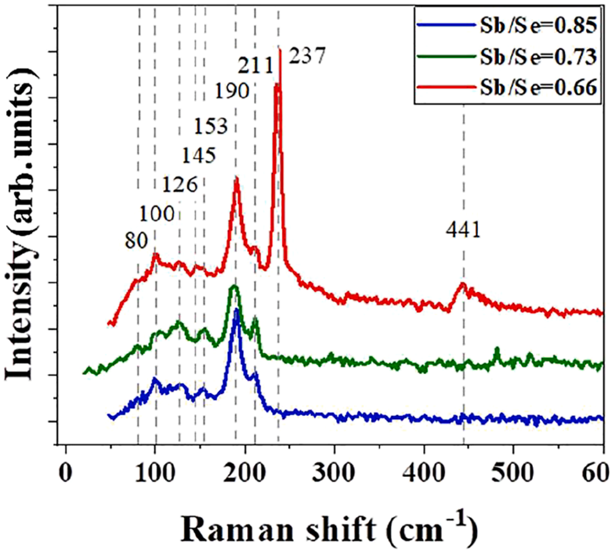

Fig. 6. Raman scattering spectra of Sb_xSe_y samples deposited with various Sb/Se ratios.

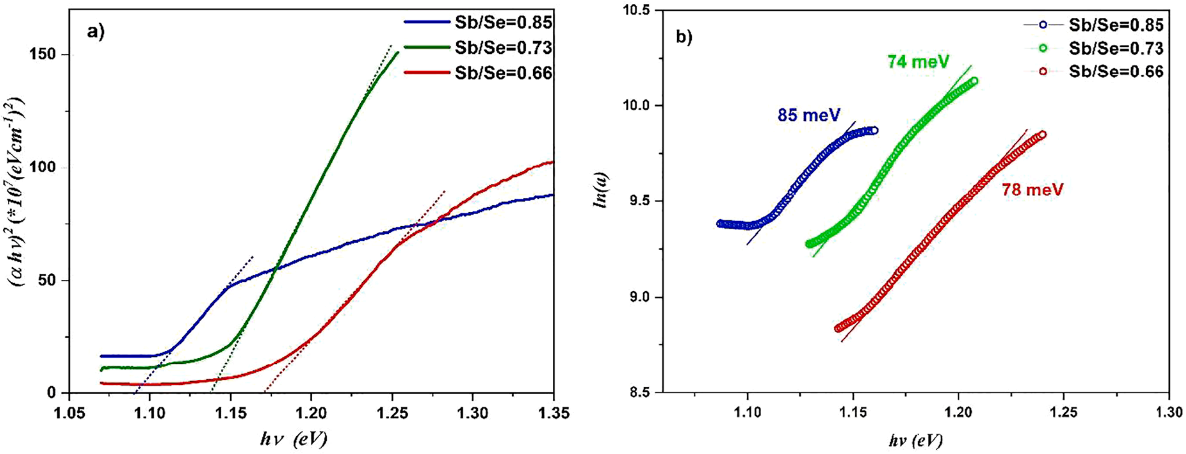

Fig.7. (a) Tauc plots of Sb_xSe_y films deposited at different ratios, (b) plot of ln(α) against photon energy (hν).

constant related to effective mass, and n is equal to 2 and 1/2 for direct and indirect bandgap semiconductors, respectively. Here, n equals 2 because Sb_2Se_3 has a direct bandgap, and E_g for various compositional thin films is determined to be 1.09, 1.14 and 1.17 eV for 0.85, 0.73 and 0.66 Sb/Se ratio samples. A slight change in the band gap width compared with pure Sb_2Se_3 thin film (1.15 eV) (Chen et al., 2015) was observed due to the change in atomic arrangement from disorder to order. These results indicate that the structural and optical properties of Sb_xSe_y thin films are closely related to the Sb/Se ratio, which is consistent with previous reports (Liang et al., 2020).

To study the structural disorder of Sb_xSe_y films, the Urbach energy (E_U) was also calculated. The existence of an exponential increase in the absorption coefficient near the band edge (Urbach tail) indicates the presence of localized states or impurity states in the band gap region that causes disturbance in the band structure of the polycrystalline films. The value of E_U indicates the level of crystallinity and structural defects present in the films. In the low photon energy range, an exponential variation in the absorption edge followed the Urbach empirical equation (Eq. (6)):

$$\alpha = \alpha_0 exp\left[\frac{h\nu}{E_U}\right] \tag{6}$$

where α_0 is a constant. The value of E_U can be obtained from the inverse slope of the linear plot of ln(α) vs hν (Fig. 7b). The lower value of E_U at elemental composition approaching the stoichiometric ratio indicates the decrease in structural defects and localized states density in the band gap region of the films.

4. Conclusions

In conclusion, we systematically studied the morphological, structural, and optical properties of Sb_2Se_3 films with different compositions produced from separate sources of Sb and Se by the CMBD method. Our CMBD method performs an excellent control to tune the band gap of Sb_2Se_3 films by changing the Sb/Se ratio during the growth process and the evaporation temperature. SEM imaging shows the surface morphology of Sb_xSe_y thin films deposited on SLG at a substrate temperature of 500 °C. All Sb_xSe_y thin films showed compact surface morphology. The average diameters and lengths of Sb_xSe_y thin film rods, which consist of a dense columnar structure grown with an angle from 0° to 60° respect the substrate, ranged between 0.5 ÷ 2 μm and 2 ÷ 10 μm, respectively. From EDX data, it was observed that the increase in Se content in the solid phase was directly proportional to the Se content in the vapour phase during the growth process. The grazing incidence X-ray diffraction study describes that Sb_2Se_3 thin films with micro-sized crystal grains exhibit (hk1) preferential orientation at the stoichiometric composition. The Raman spectroscopy measurement shows that there is a blueshift of most of the Raman peaks of Sb_2Se_3 samples; as a result, we can conclude that there might be a slight amount of compressive strain present in the film structure. The direct band gap obtained from Tauc's plot indicate that deposited Sb_2Se_3 films are suitable for thin-film photovoltaics. Calculated value of the Urbach energy indicates low density of localized states in the band gap region for Sb_xSe_y films, synthesized with an elemental ratio close to stoichiometry.

Declaration of Competing Interest

The authors declare that they have no known competing financial interests or personal relationships that could have appeared to influence the work reported in this paper.

Acknowledgements

This work was supported by the Ministry of innovative development of the Republic of Uzbekistan (Grant № MRB-2021-540) and the State Committee on Science and Technology of the Republic of Belarus (Grant No: F21UZBG-022).

References

Chen, C., Li, W., Zhou, Y., Chen, C., Luo, M., Liu, X., Zeng, K., Yang, B., Zhang, C., Han, J., Tang, J., 2015. Optical properties of amorphous and polycrystalline Sb_2Se_3 thin films prepared by thermal evaporation. Appl. Phys. Lett. 107 https://doi.org/10.1063/1.4927741.

Chen, C., Bobela, D.C., Yang, Y., Lu, S., Zeng, K., Ge, C., Yang, B., Gao, L., Zhao, Y., Beard, M.C., Tang, J., 2017. Characterization of basic physical properties of Sb_2Se_3 and its relevance for photovoltaics. Front. Optoelectron. 10, 18–30. https://doi.org/10.1007/s12200-017-0702-z.

Choi, Y.C., Mandal, T.N., Yang, W.S., Lee, Y.H., Im, S.H., Noh, J.H., Seokil, S., 2014. Sb_2Se_3 -Sensitized Inorganic-Organic Heterojunction Solar Cells Fabricated Using a Single-Source Precursor. Angewandte Chemie 126, 1353–1357. https://doi.org/10.1002/ange.201308331.

Deringer, V.L., Stoffel, R.P., Wuttig, M., Dronskowski, R., 2015. Vibrational properties and bonding nature of Sb_2Se_3 and their implications for chalcogenide materials. Chem. Sci. 6, 5255–5262. https://doi.org/10.1039/c5sc00825e.

Filip, M.R., Patrick, C.E., Giustino, F., 2013. GW quasiparticle band structures of stibnite, antimonselite, bismuthinite, and guanajuatite. Phys. Rev. B. 87, 205125 https://doi.org/10.1103/PhysRevB.87.205125.

Gadelmawla, E.S., Koura, M.M., Maksoud, T.M.A., Elewa, I.M., Soliman, H.H., 2002. Roughness parameters. J. Mater. Process. Technol. 123, 133–145. https://doi.org/10.1016/S0924-0136(02)00060-2.

Guo, H., Chen, Z., Wang, X., Cang, Q., Jia, X., Ma, C., Yuan, N., Ding, J., 2019. Enhancement in the Efficiency of Sb_2Se_3 Thin-Film Solar Cells by Increasing Carrier Concertation and Inducing Columnar Growth of the Grains. Solar RRL 3. https://doi.org/10.1002/solr.201800224.

Kim, J., Yang, W., Oh, Y., Lee, H., Lee, S., Shin, H., Kim, J., Moon, J., 2017. Self-oriented Sb_2Se_3 nanoneedle photocathodes for water splitting obtained by a simple spin-coating method. J. Mater. Chem. A Mater. 5, 2180–2187. https://doi.org/10.1039/c6ta09602f.

Kumar, A., Kumar, V., Romeo, A., Wiemer, C., Mariotto, G., 2021. Raman Spectroscopy andIn SituXRD Probing of the Thermal Decomposition of Sb_2Se_3 Thin Films. J. Phys. Chem. C 125, 19858–19865. https://doi.org/10.1021/acs.jpcc.1c05047.

Lei, H., Chen, J., Tan, Z., Fang, G., 2019. Review of Recent Progress in Antimony Chalcogenide-Based Solar Cells: Materials and Devices. Solar RRL. https://doi.org/10.1002/solr.201900026.

Li, Z., Chen, X., Zhu, H., Chen, J., Guo, Y., Zhang, C., Zhang, W., Niu, X., Mai, Y., 2017. Sb_2Se_3 thin film solar cells in substrate configuration and the back contact selenization. Solar Energy Mater. Solar Cells 161, 190–196. https://doi.org/10.1016/j.solmat.2016.11.033.

Li, Z., Liang, X., Li, G., Liu, H., Zhang, H., Guo, J., Chen, J., Shen, K., San, X., Yu, W., Schropp, R.E.I., Mai, Y., 2019. 9.2%-efficient core-shell structured antimony selenide nanorod array solar cells. Nat. Commun. 10 https://doi.org/10.1038/s41467-018-07903-6.

Liang, G.X., di Luo, Y., Chen, S., Tang, R., Zheng, Z.H., Li, X.J., Liu, X.S., Liu, Y.K., Li, Y. F., Chen, X.Y., Su, Z.H., Zhang, X.H., Ma, H.L., Fan, P., 2020. Sputtered and selenized Sb_2Se_3 thin-film solar cells with open-circuit voltage exceeding 500 mV. Nano Energy 73. https://doi.org/10.1016/j.nanoen.2020.104806.

Ma, C., Guo, H., Wang, X., Chen, Z., Cang, Q., Jia, X., Li, Y., Yuan, N., Ding, J., 2019. Fabrication of Sb_2Se_3 thin film solar cells by co-sputtering of Sb_2Se_3 and Se targets. Solar Energy 193, 275–282. https://doi.org/10.1016/j.solener.2019.09.046.

Maghraoui-Meherzi, H., ben Nasr, T., Dachraoui, M., 2013. Synthesis, structure and optical properties of Sb_2Se_3. Mater. Sci. Semicond. Process 16, 179–184. https://doi.org/10.1016/j.mssp.2012.04.019.

Mavlonov, A., Razykov, T., Raziq, F., Gan, J., Chantana, J., Kawano, Y., Nishimura, T., Wei, H., Zakutayev, A., Minemoto, T., Zu, X., Li, S., Qiao, L., 2020a. A review of Sb_2Se_3 photovoltaic absorber materials and thin-film solar cells. Solar Energy. https://doi.org/10.1016/j.solener.2020.03.009.

Mavlonov, A., Shukurov, A., Raziq, F., Wei, H., Kuchkarov, K., Ergashev, B., Razykov, T., Qiao, L., 2020b. Structural and morphological properties of PLD Sb_2Se_3 thin films for use in solar cells. Solar Energy 208, 451–456. https://doi.org/10.1016/j.solener.2020.08.004.

Nagata, K., Ishibashi, K., Miyamoto, Y., 1981. Raman and Infrared Spectra of Rhombohedral Selenium. Japan. J. Appl. Phys. To.

Razykov, T.M., Shukurov, A.K., Kuchkarov, K.M., Ergashev, B.A., Khurramov, R.R., Bekmirzoyev, J.G., Mavlonov, A.A., 2019. Morphological and Structural Characteristics of Sb_2Se_3 Thin Films Fabricated by Chemical Molecular Beam Deposition. Appl. Solar Energy (English translation of Geliotekhnika) 55, 376–379. https://doi.org/10.3103/S0003701X19060094.

Rühle, S., 2016. Tabulated values of the Shockley-Queisser limit for single junction solar cells. Solar Energy 130, 139–147. https://doi.org/10.1016/j.solener.2016.02.015.

Shongalova, A., Correia, M.R., Teixeira, J.P., Leitão, J.P., González, J.C., Ranjbar, S., Garud, S., Vermang, B., Cunha, J.M.V., Salomé, P.M.P., Fernandes, P.A., 2018a. Growth of Sb_2Se_3 thin films by selenization of RF sputtered binary precursors. Solar Energy Mater. Solar Cells 187, 219–226. https://doi.org/10.1016/j.solmat.2018.08.003.

Shongalova, A., Correia, M.R., Vermang, B., Cunha, J.M.V., Salomé, P.M.P., Fernandes, P.A., 2018b. On the identification of Sb_2Se_3 using Raman scattering. MRS Commun. 8, 865–870. https://doi.org/10.1557/mrc.2018.94.

Spalatu, N., Krautmann, R., Katerski, A., Karber, E., Josepson, R., Hiie, J., Acik, I.O., Krunks, M., 2021. Screening and optimization of processing temperature for Sb_2Se_3 thin film growth protocol: Interrelation between grain structure, interface intermixing and solar cell performance. Solar Energy Mater. Solar Cells 225. https://doi.org/10.1016/j.solmat.2021.111045.

Vidal-Fuentes, P., Guc, M., Alcobe, X., Jawhari, T., Placidi, M., Pérez-Rodríguez, A., Saucedo, E., Roca, V.I., 2019. Multiwavelength excitation Raman scattering study of Sb_2Se_3 compound: fundamental vibrational properties and secondary phases detection. 2d Mater 6, 045054. https://doi.org/10.1088/2053-1583/ab4029.

Wang, L., Li, D.B., Li, K., Chen, C., Deng, H.X., Gao, L., Zhao, Y., Jiang, F., Li, L., Huang, F., He, Y., Song, H., Niu, G., Tang, J., 2017. Stable 6%-efficient Sb_2Se_3 solar cells with a ZnO buffer layer. Nat. Energy 2. https://doi.org/10.1038/nenergy.2017.46.

Wen, X., Chen, C., Lu, S., Li, K., Kondrotas, R., Zhao, Y., Chen, W., Gao, L., Wang, C., Zhang, J., Niu, G., Tang, J., 2018. Vapor transport deposition of antimony selenide thin film solar cells with 7.6% efficiency. Nat. Commun. 9 https://doi.org/10.1038/s41467-018-04634-6.

Yang, K., Li, B., Zeng, G., 2020. Effects of substrate temperature and SnO_2 high resistive layer on Sb_2Se_3 thin film solar cells prepared by pulsed laser deposition. Solar Energy Mater. Solar Cells 208. https://doi.org/10.1016/j.solmat.2019.110381.

Zeng, K., Xue, D.J., Tang, J., 2016. Antimony selenide thin-film solar cells. Semicond. Sci. Technol. https://doi.org/10.1088/0268-1242/31/6/063001.

Zhang, L., Wu, K., Yu, J., Yu, Y., Wei, Y., 2021. Sb_2Se_3 films fabricated by thermal evaporation and post annealing. Vacuum 183. https://doi.org/10.1016/j.vacuum.2020.109840.

Zhou, Y., Leng, M., Xia, Z., Zhong, J., Song, H., Liu, X., Yang, B., Zhang, J., Chen, J., Zhou, K., Han, J., Cheng, Y., Tang, J., 2014. Solution-processed antimony selenide heterojunction solar cells. Adv. Energy Mater. 4 https://doi.org/10.1002/aenm.201301846.

Zhou, Y., Wang, L., Chen, S., Qin, S., Liu, X., Chen, J., Xue, D.J., Luo, M., Cao, Y., Cheng, Y., Sargent, E.H., Tang, J., 2015. Thin-film Sb_2Se_3 photovoltaics with oriented one-dimensional ribbons and benign grain boundaries. Nat. Photonics 9, 409–415. https://doi.org/10.1038/nphoton.2015.78.